R-04-36

Integrated near-field evolution model for a KBS-3 repository

Allan Hedin
Svensk Kärnbränslehantering AB

August 2004

Svensk Kärnbränslehantering AB
Swedish Nuclear Fuel
and Waste Management Co
Box 5864
SE-102 40 Stockholm Sweden
Tel 08-459 84 00
+46 8 459 84 00
Fax 08-661 57 19
+46 8 661 57 19

ISSN 1402-3091
SKB Rapport R-04-36

Integrated near-field evolution model for a KBS-3 repository

Allan Hedin
Svensk Kärnbränslehantering AB

August 2004

Preface

This report presents the first version of an integrated near-field evolution model for a KBS-3 repository.

Ivars Neretnieks at the Royal Institute of Technology, Stockholm, Ola Karnland, Lennart Börgesson and Harald Hökmark at Clay Technology AB and David Arcos at Enviros, Barcelona are gratefully acknowledged for comments on this report and for providing benchmarking data.

Stockholm, August 2004

Allan Hedin

Summary

A model for the integrated treatment of a number of processes determining the long-term evolution of a KBS-3 repository for spent nuclear fuel is presented. The integrated system model reproduces several important results obtained with a number of different process level models in SKB's latest safety assessment. Examples include the evolutions of the temperature in the fuel rods, the canister, the buffer and the host rock, of the buffer chemical composition, of canister corrosion and of the interior of an assumed defective canister. The mechanistic understanding and mathematical description of the processes underlying the evolution is the same as for the process models but the methods for quantifying the processes have been adapted to the particular problems at hand to increase calculation speed and all sub-models are handled in a common framework. The model executes in around one second, making it a potentially useful tool for comprehensive evaluations in coming safety assessments.

Contents

1 Introduction

The KBS-3 concept for storage of spent nuclear fuel, where copper canisters with a cast iron insert containing spent nuclear fuel are surrounded by bentonite clay and deposited at approximately 500 m depth in saturated, granitic rock, Figure 1-1, has been studied extensively for more than 20 years. The processes behind the long-term evolution of the canister, buffer, backfill and rock have been studied in laboratory experiments, field observations and by model calculations. Examples include chemical degradation of the buffer and canister, the thermal evolution of the repository as well as groundwater chemistry, flow and transport processes. The results are used in integrated safety assessments, evaluating the long-term safety of the system /SKB, 1999/. These require a description of the long-term evolution of the repository taking into account both all relevant processes within the system and the varying external conditions that may affect the repository. Radionuclide transport and dose calculations are at the core of the evaluations as are assessments of the long-term isolating potential of the copper canister.

The system of coupled processes behind the long-term evolution is complex. In the mathematical modelling of the repository, the process system is therefore studied with a number of different process models, each illustrating certain aspects of the total evolution. Frequently, the focus in these models is on either thermal, hydraulic, mechanical or chemical processes. The full integration of all aspects of the evolution is normally done by reasoning around the process model results in a safety report.

Here, a newly developed system model for the near-field evolution, consisting of several integrated sub-models, each mimicking a near-field process model, is presented. The equations solved by a particular sub-model are the same as those handled by the corresponding process model. The system model thus builds on the same mechanistic understanding as the process models but the methods for solving the equations have been adapted to the problems at hand rather than utilising general purpose codes. The set of process models mimicked is not complete, excluding e.g. the short-term saturation model of the buffer where couplings between processes are strong and detailed hydromodelling of the heterogeneous, fractured host rock.

The KBS-3 concept is primarily aiming at complete isolation of the waste, achieved by the integrity of the copper canisters. This first version of the system model is therefore not concerned with radionuclide releases and transport. A simplified description of also these phenomena has been reported earlier /Hedin, 2002/ and can possibly be incorporated into future versions of the system model.

Time-dependent output from one sub-model is in general not used directly as input to another model in the present version. Most dependencies of this kind are weak for the modelled situations, and the time-scales of relevance are often different for the different sub-models, facilitating a simplified handling of links between the models.

A main reason for the development reported here is to obtain an integrated treatment of the most significant processes in the long-term repository evolution, ensuring that a consistent input database is used in modelling all aspects of the evolution. Furthermore, the integrated modelling tool is controlled directly by the safety analyst rather than by a number of distributed expert groups. As will be demonstrated below, several measures have been taken to increase calculation speed. This allows for rapid evaluation of a number of

different sets of input data and also for probabilistic evaluations. The model can be executed probabilistically, but only deterministic results will be presented here since the database for probabilistic calculations is still insufficient.

Other reasons for the development are to gain insight into the relative importance of various processes and assumptions at a holistic level and to provide quality assurance through an independent set of models for crucial aspects of the near-field evolution. The ambition is however not to replace the more detailed process models. These will always be needed to fully account for all details in the mechanisms behind individual processes and as a necessary basis for the development of simplified models. Also, the expertise behind the development of the process models is required to describe and justify the common scientific basis for both types of models.

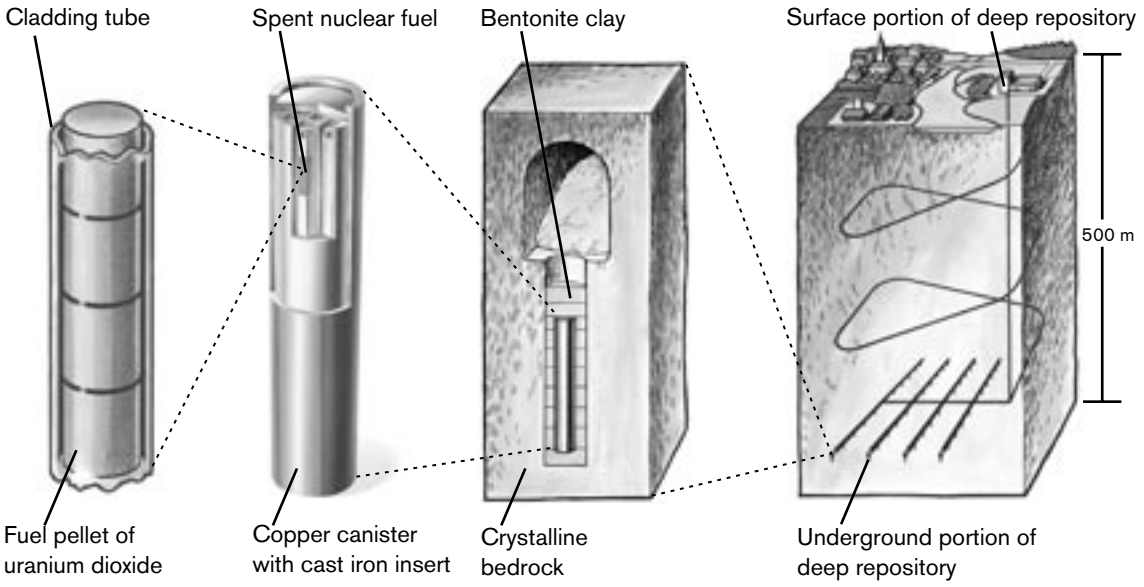

Figure 1-1. *The KBS-3 concept for storage of spent nuclear fuel.*

2 System model overview

Figure 2-1 shows the set of process models that have been included as sub-models in the system model and how the sub-models are linked. Most of these links are however not automated in the present version of the model. The following is a brief description of each sub-model in Figure 2-1. Detailed descriptions and benchmarking results are given in Appendices.

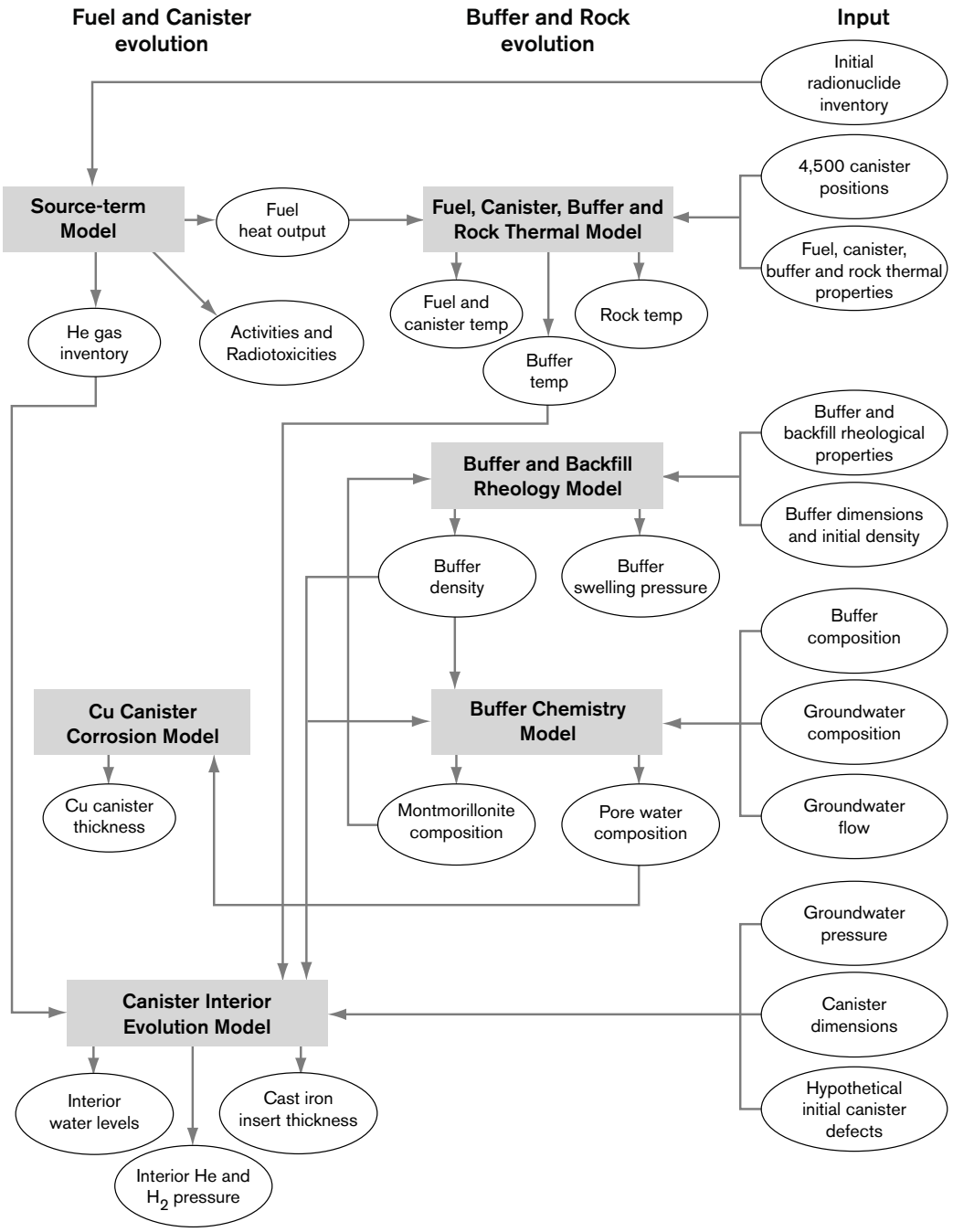

Figure 2-1. *The system model with sub-models represented as rectangles; input data and time-dependent calculation results as ellipses.*

2.1 The source-term sub-model

The evolution of the initial radioactive inventory of the spent fuel is readily calculated using the exponential decay law and Bateman's equations for chain decay /Bateman, 1908/. There is no difference between this sub-model and any process model handling the temporal evolution of the radioactive inventory. The heat output for the thermal model is obtained from the activities and decay energies of the radioactive nuclides. To facilitate the thermal modelling (see below), the heat output as a function of time is approximated by a sum of a few exponential terms fitted to the results of the decay model.

2.2 The thermal sub-model

The thermal sub-model calculates the temperature increase as a function of time in any specified point in the host rock due to the presence of the heat generating fuel in the repository. It also calculates the buffer temperature at the mid-height of the canister as a function of radial distance from the canister wall and time for any specified canister. Furthermore, the temperatures of the copper canister, the cast iron insert, the fuel boxes and of the fuel rods are calculated in a one-dimensional approximation. The locations of the typically 4750 canisters, the heat output of the canisters as a function of time and the thermal properties of the fuel, the canister, the buffer, the rock materials and of the interfaces between these components are essential input data to this sub-model. The model and benchmarking results are further described in Appendix A.

2.3 The buffer and backfill rheology sub-model

At deposition, the buffer is not in hydraulic equilibrium with the surrounding, saturated rock. Saturation of the buffer will typically occur within a few tens of years but may take considerably longer, depending on the water supply from the fractured rock surrounding the deposition hole and from the deposition tunnel backfill on top of the buffer. At the end of the saturation process, a swelling pressure will develop in the buffer and the buffer will expand upwards and compress the backfill to some extent. Due to friction against the walls of the deposition hole, the expansion of the buffer will finally result in a gradually decreasing density in the top part of the buffer. The details of the swelling process are not important to the long-term safety, if only the final density distribution of the buffer after swelling can be determined and if it can be demonstrated that the buffer will not be harmed in any other way by the saturation process.

The final density distribution can be approximately obtained by a numerical equilibrium calculation where the upward expansion of the buffer is balanced by friction against the walls of the deposition hole and the force exerted on the buffer by the compressed backfill. The calculation involves the relationship between buffer swelling pressure and density, the friction angle between buffer and rock and the compression properties of the backfill /Börgesson, 1982/. The numerical solution to the equilibrium equation is obtained in a few iterations. Process models /Börgesson and Hernelind, 1999/, which are concerned with not only the final state of the saturation phase but with the entire evolution leading to it, are considerably more computationally demanding. An advantage of the system sub-model is that the relation between swelling pressure and density can readily be modified. Modified relationships, which take into account the effect of groundwater salinity /Karnland et al, 2002/ have been incorporated into that model. A more detailed account of the model and benchmarking results is given in Appendix B.

2.4 The buffer chemistry sub-model

This sub-model simulates the evolution, in a million year perspective, of the buffer chemistry due to the continuous, slow diffusion controlled exchange of dissolved species between the buffer pore water and the groundwater. Dissolution of and reactions involving accessory minerals originally present in the buffer and exchange of ionic species adsorbed to the montmorillonite clay fraction of the buffer and those dissolved in the buffer pore water is treated. The buffer is modelled as a mixed tank and this feature as well as the understanding of the chemical evolution is entirely based on the corresponding process model /Bruno et al, 1999/. The evolution is modelled in a number of consecutive time steps of typically several thousand years as determined by the slow groundwater flow around the deposition hole and the diffusion properties of the buffer/groundwater interface. In each time step, the pore water is completely replaced by groundwater and the resulting chemical equilibrium is calculated. A calculation algorithm specifically designed for the particular equilibrium calculation was developed for this sub-model, see Appendix C for a more detailed account and benchmarking calculations. The process model /Bruno et al, 1999/ solves the same problem with a general purpose code requiring considerably more computer time. It should be noted that the process model has recently been expanded to also include detailed transport within the buffer, a more developed treatment of accessory minerals and temperature dependence /Arcos et al, 2000/. The latter is important for the modelling of the initial 1000 years when the buffer temperature is elevated and varies over the buffer volume.

The detailed spatial and temporal characteristics of the evolving state of the buffer as it interacts with groundwater are not captured with this simplified sub-model, mainly since diffusion in the buffer is by-passed with the mixed tank approximation. In many cases, the diffusion occurs on a shorter time-scale than the processes describing the exchange of species between the buffer pore-water and the groundwater, thus justifying the tank approximation, but the situation is complicated by the coupling to chemical reactions and the fact that anions and cations have different transport properties in the buffer. Furthermore, the hydraulic boundary conditions, which are crucial for the overall time scale of the chemical evolution, will vary considerably between deposition holes. This means that also the time scale for reaching chemical equilibrium between the buffer and a groundwater of assumed constant composition could vary from tens of thousands of years to beyond several million years. The purpose of the model is however to describe the chemical states that the buffer will traverse on its way to equilibrium with a specific groundwater composition, in order to determine whether the safety-related buffer properties are acceptable for this continuum of states. In particular, it is important to elucidate the ion exchange state and pH. The detailed temporal and spatial pathway to this equilibrium is of secondary concern. The model is therefore seen as a useful approximation for its purposes.

2.5 The copper corrosion sub-model

Copper is a highly stable metal in Swedish granitic groundwaters. The slow corrosion due to the low concentrations of corrodants in the slowly moving groundwater and diffusion controlled transport in the buffer is calculated with simple mass balance considerations in process models. These are directly adopted in the system sub-model as are expressions for corrosion due to impurities initially present in the buffer. The natural variability of the groundwater flow as calculated in geohydrological models of a particular site is readily taken into account in the sub-model. See further Appendix D.

2.6 The canister interior sub-model

This sub-model treats the internal hydrochemical evolution of a canister with an assumed penetrating defect. The model handles water ingress from the buffer, driven by the pressure difference between the groundwater and the canister interior, build-up of water, both in the annulus between copper canister and the cast iron insert and inside the insert, and anaerobic corrosion of the insert leading to hydrogen gas formation and a consequent build-up of an internal gas pressure. The model and benchmarking calculations are briefly described in Appendix E.

2.7 Integration

From the point of view of integration, the main advantage of the system model is that it provides a consistent input database for all sub-models and allows for rapid calculations of a number of input data variations, thus providing information on input data sensitivities.

Regarding transfer of results between models, the arrows in Figure 2-1 indicate how results from a particular sub-model are, or could be, used by other models. Tough in the present version several of these dependencies are not implemented, it is possible to evaluate the potential impact of the dependencies using the system model. In several cases, the model can be used to substantiate claims that dependencies are not important. The buffer chemistry model is e.g. valid in a 10^3–10^6 year perspective and it is readily demonstrated that the buffer temperature will be virtually equal to the rock background temperature in this time perspective. Furthermore, for the purposes of the safety assessment, it is often fully sufficient to demonstrate that the calculated quantities lie within certain limits yielding the desired performance of the system, rather than establishing exact values. This concerns e.g. the canister and buffer temperatures as well as the buffer density, chemical composition, hydraulic conductivity and swelling pressure.

2.8 Performance

The system sub-models and the corresponding process models in Figure 2-1 solve essentially the same equations except for the buffer and backfill rheology model. Compared to the process models, calculation speed is gained by (see Appendices for details)

- the economic use of pre-calculated results (the thermal model),
- by-passing details in the short-term saturation phase of the buffer, focussing instead on the final state of this phase (the buffer and backfill rheology model),
- the development of a tailor-made calculation scheme for a chemical equilibrium problem, normally solved with a general purpose code (the buffer chemistry model) and
- use of an explicit rather than an implicit solution method in combination with an increased time step facilitated by the introduction of damping features to prevent oscillations (the canister interior model).

Due to the increased computation efficiency, the whole system model is executed in less than one second on a 1.5 GHz Personal Computer, yielding estimates of crucial aspects of the system evolution in a million year perspective.

3 Discussion

The first aim with this system model has been to reproduce results obtained with a number of process models treating sub-systems or isolated aspects of the entire system evolution. This benchmarking is essential for the confidence in the system model. The discrepancies observed in the benchmarking exercises are too small to affect the usefulness of the model for long-term safety evaluations.

There are a number of relevant aspects of the evolution that can not readily be included in a model of this type. Examples include the complex thermo-hydro-mechanical evolution of the clay buffer while it saturates shortly after deposition and groundwater flow and transport in the highly heterogeneous fractured host rock. The groundwater flow is though coupled to the integrated model through the use of results from separate hydro calculations.

This paper has also demonstrated that much of the near-field evolution can be expressed in mathematically relatively simple terms, yielding insights into the complexity of the problem at hand.

It is concluded that the model will help in evaluating long-term barrier evolution in a more rigorous and consistent manner, increase transparency in the safety assessment, help the analyst by providing rapid answers regarding the effects on long-term safety of various assumptions concerning the initial state and long-term processes of the repository, and pin-point in a consistent manner crucial data uncertainties. Sensitivity studies with the system model could also identify needs for more systematic studies with a detailed process model.

4 References

Abramowitz M, Stegun I A, 1970. Handbook of Mathematical Functions, ISBN 0-486-61272-4, Dover.

Ageskog L, Jansson P, 1999. Heat Propagation In and Around the Deep Repository, SKB TR-99-02, Svensk Kärnbränslehantering AB.

Arcos D, Bruno J, Benbow S, Takase H, 2000. Behaviour of Bentonite Accessory Minerals during the Thermal Stage, SKB TR-00-06, Svensk Kärnbränslehantering AB.

Bateman H, 1908. The Solution of a System of Differential Equations Occurring in the Theory of Radio-Active Transformations, Proc. Camb. Phils. Soc., 15 423 (1908-1910).

Bond A E, Hoch A R, Jones G D, Tomczyk A J, Wiggin R M, Worracker W J, 1997. Assessment of a Spent Fuel Disposal Canister, SKB TR-97-19, Svensk Kärnbränslehantering AB.

Bruno J, Arcos D, Duro L, 1999. Processes and Features Affecting the Near Field Hydrochemistry, SKB TR-99-29, Svensk Kärnbränslehantering AB.

Börgesson L, 1982. Buffer Mass Test − Predictions of the Behaviour of the Bentonite-Based Buffer Materials, STRIPA Project Report 82-08, Svensk Kärnbränsleförsörjning.

Börgesson L, Hernelind J, 1999. Coupled Thermo-Hydro-Mechanical Calculations of the Water Saturation Phase of a KBS-3 Deposition Hole, SKB TR-99-41, Svensk Kärnbränslehantering AB.

Börgesson L, 2004. Clay Technology AB, Lund Sweden, personal communication.

Carslaw H S, Jaeger J C, 1959. Conduction of Heat in Solids, Oxford University Press, New York.

Davies C W, 1962. Ion Association, Butterworths, London.

Hedin A, 2002. Integrated Analytic Radionuclide Transport Model for a Spent Nuclear Fuel Repository in Saturated Fractured Rock, Nuclear Technology 138 2 179.

Hökmark H, Fälth B, 2003. Thermal dimensioning of the deep repository SKB TR-03-09, Svensk Kärnbränslehantering AB.

Hökmark H, Claesson J, 2004. Use of an Analytical Solution for Calculating Temperatures in Repository Host Rock. Accepted for publication in Engineering Geology.

Karnland O, Muurinen A, Karlsson F, 2002. Bentonite swelling pressure in NaCl solutions – Experimentally determined data and model calculations. Sitges Symposium on large scale field tests in granite. November 12–14, 2003. University of Catalonia, Spain.

Neretnieks I, 1979. Transport Mechanism and Rates of Transport of Radionuclides in the Geosphere as Related to the Swedish KBS-Concept, Proc. Symp. Underground Disposal of Radioactive Wastes, Otaniemi, Finland, July 2-6, 1979, Vol II. p 108, International Atomic Energy Agency.

Neretnieks I, 1986a. Stationary Transport of Dissolved Species in the Backfill Surrounding a Waste Canister in Fissured Rock: Some Simple Analytical Solutions, Nuclear Technology, 72, 196.

Neretnieks I, 1986b. Some Uses of Natural Analogues in Assessing the Function of a HLW Repository, Chemical Geology, 55, p. 175.

Renström P, 1997. Calculation of the fuel temperature in vacuous storage canisters made of copper with cast steel insert SKB PPM 97-3420-23, Svensk Kärnbränslehantering AB.

SKB, 1999. Deep repository for spent nuclear fuel; SR 97 − Post-closure safety. Parts I and II. SKB TR-99-06, Svensk Kärnbränslehantering AB.

Appendix A

The thermal sub-model

A.1 Host rock temperature

For calculation of the temperature at a specified point (x_0, y_0, z_0) in the host rock, canisters farther away than a few times the canister height (4.8 m) can be regarded as point sources. The temperature increase, ΔT, is obtained as a sum over all canisters of a convolution integral involving the time dependent source term, $q(t)$, and the Green's function describing the thermal response to a unit heat pulse at a distance R from (x_0, y_0, z_0) /Carslaw and Jaeger, 1959/:

$$\Delta T = \frac{1}{8(\pi\kappa)^{3/2}\rho C_p}\int_0^t q(\tau)(t-\tau)^{-3/2}\exp\left(-\frac{R^2}{4\kappa(t-\tau)}\right)d\tau \quad (1)$$

where κ is the thermal diffusivity, ρ the density and C_p the specific heat of the rock. For exponentially decaying source terms, the integral must be evaluated numerically. For any given source term, the integral depends only on the time after deposition, t, and the ratio

$$a = R^2 / 4\kappa \quad (2)$$

The temperature increase at the surface (z = 0) is taken to be zero and this boundary condition is satisfied by adding a negative mirror image source term at (x, y, -z) for a canister located at (x, y, z), see e.g. /Carslaw and Jaeger, 1959/ for a more detailed account of the technique. The source term $q(t)$ is not obtained directly from the source term model described above, but rather as a fit of a sum of exponentials to the calculated residual power as a function of time. For e.g. a boiling water reactor (BWR) fuel of burn-up 38 MWd/tonne deposited after 40 years of interim storage, the following expression is a good approximation over at lest 10,000 years /Hökmark and Fälth, 2003/:

$$q(t) = P_0\left(0.07e^{-t/20}+0.713e^{-t/50}-0.051e^{-t/200}+0.231e^{-t/500}+0.024e^{-t/2000} -0.009e^{-t/5000}+0.022e^{-t/20000}\right) \quad (3)$$

where P_0 denotes the residual power at the time of deposition. In solving the integral in Equation (1), each term in the sum of exponentials was evaluated separately and then added, using the variable substitution

$$s = \sqrt{(t-\tau)/t_0} \quad (4)$$

when evaluating the integrals. Here, t_0 denotes the time constants in the exponential terms. The substitution yields a better conditioned numerical problem.

An important endpoint in the thermal calculations is the peak canister temperature that, for symmetry reasons, will occur at canister mid-height. Thus also the deposition hole rock wall temperature at canister mid-height needs to be accurately determined.

Therefore, canisters closer to (x_0, y_0, z_0) than 14 meters are divided into 20 equal segments, each represented by a point source. A finer division did not change the results in any significant way. The accuracy of calculated rock temperatures near canisters was further increased by a simple redistribution of the heat power between the 20 point sources, to account for the uneven heat flux distribution due to the finite size of the cylindrical canister. Rather than assigning all 20 sources 1/20 of the canister heat power, the two outer points are each given the fraction 2.59/20 and the remaining 18 points 0.823/20. These values were obtained from a comparison between an analytical and a numerical model /Hökmark and Fälth, 2003/.

The treatment neglects the presence of the tunnel backfill above the deposition hole, but this has been demonstrated to influence the critical temperature marginally /Hökmark and Fälth, 2003/.

Two measures are taken to radically increase the calculation speed:

1. For the source term of concern, the integral in Equation (1) is pre-calculated for a number of combinations of a and t covering together the range of interest of these two parameters. The so created look-up table is used to evaluate the integral in the actual calculation cases. It was demonstrated that 80 x 80 pre-calculated values covering $0.01 < t < 10^6$ years and a values corresponding to distances in the interval $0.1 < R < 5000$ m for typical values of κ, yields a sufficient accuracy.

2. The efficiency of the calculations is also improved by dividing the geosphere into a number of concentric shells centred at (x_0, y_0, z_0). The number of canisters within each shell is counted and only one integral evaluation per shell is required rather than one per canister. This is possible since the temperature increase at (x_0, y_0, z_0) depends spatially only on the distance to the heat source. A division of space into typically 50 shells, reducing the number of table interpolations by a factor of about 100, gives a sufficient accuracy.

The above measures yield a fast model that can manage an irregular spatial distribution of canisters, in contrast to several other simplified solutions that utilise the symmetry properties of a regular layout.

A.2 Buffer temperature

For reasons given above, also the buffer temperature at canister mid-height is of particular interest. Here, the heat flux from the canister is radial and will, from a few days after deposition, obey the same decay law as the heat source inside the canister. This implies that the buffer temperature at mid-height as a function of radius and time can be readily calculated with steady state heat transfer expressions once the rock temperature at the buffer/rock interface and the radial heat flux from the canister has been determined /Hökmark and Fälth, 2003/.

The average heat flux across the inner buffer surface, φ_{Buff}, assuming a 0.01 m gap, d_{CuBuff}, between the canister lateral surface and buffer is

$$\varphi_{Buff} = \frac{q(t)}{2\pi\left(\left(r_{can} + d_{CuBuff}\right)h_{can} + \left(r_{can} + d_{CuBuff}\right)^2\right)} \tag{5}$$

This expression slightly overestimates the flux at canister mid-height. Numerical calculations /Hökmark and Fälth, 2003/ indicate that it is approximately $0.92\varphi_{Buff}$. The buffer temperature at canister mid-height is obtained as

$$T_{Buff} = T_{Rock} + 0.92\varphi_{Buff}\frac{r}{\lambda_{Buff}}\ln\left(\frac{r_{Dephole}}{r}\right); \qquad r_{Can} + d_{CuBuff} < r < r_{Dephole} \tag{6}$$

A.3 Benchmarking rock and buffer temperatures

For a repository with 4000 canisters separated by 7.5 m along 25 deposition tunnels 40 m apart at z = –500 m, the temperature was calculated at the buffer/rock interface and buffer inner surface at canister mid-height for a centrally located canister. The calculation was done with the thermal sub-model and compared with results from a finite element process model /Ageskog and Jansson, 1999/, with good agreement, see Figure A-1. The difference in peak temperature is about one degree. Long-term results for the buffer/rock interface /Hökmark and Claesson, 2004/ obtained with the 3DEC code and with alternative, independent analytical solution schemes have also been well reproduced.

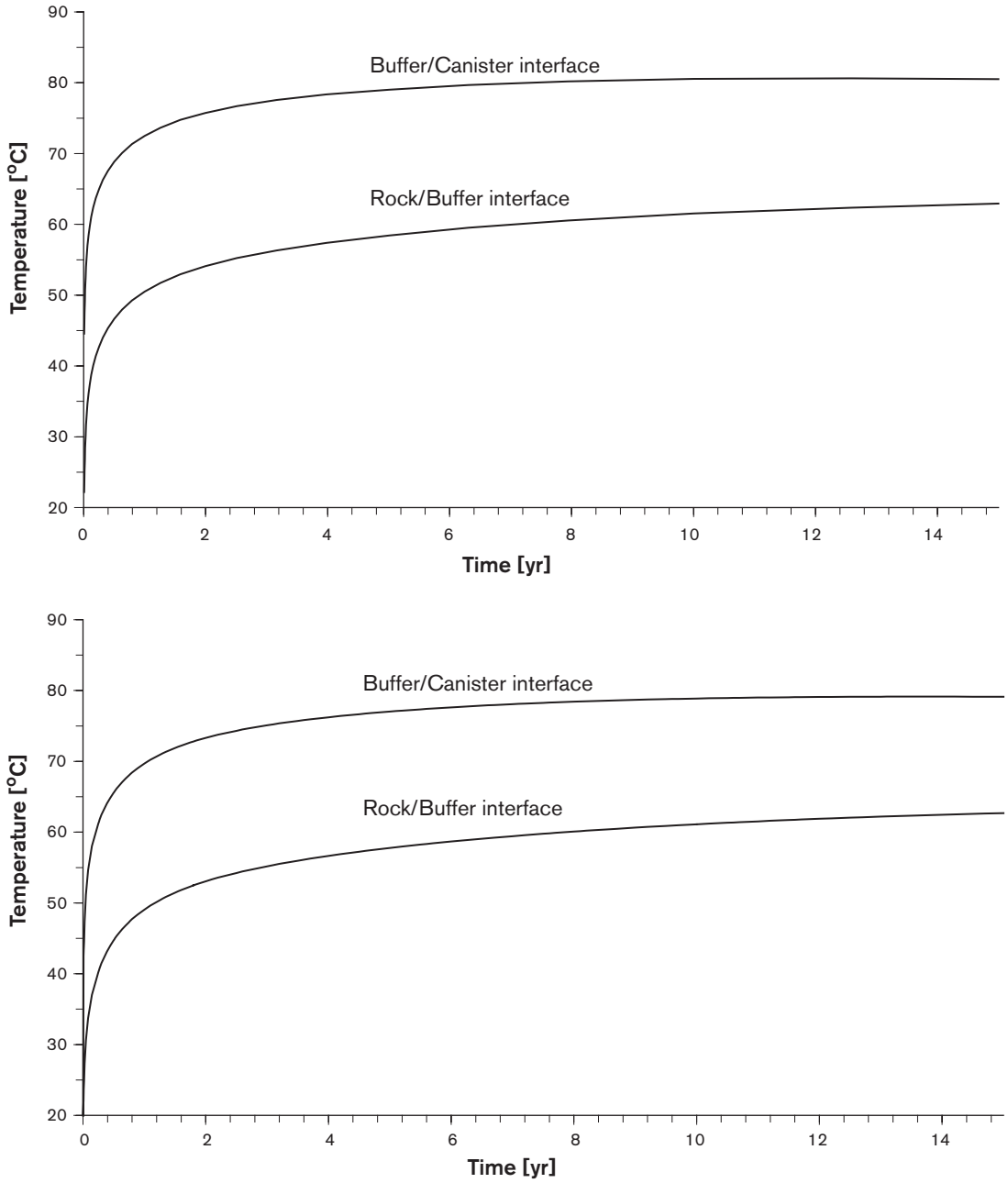

Figure A-1. *Thermal model benchmarking results for system sub-model (upper) and process model (lower).*

A.4 Canister and fuel temperatures

A.4.1 Heat transfer across gaps

When the temperature of the inner buffer surface has been determined, the calculation of canister and fuel temperatures essentially amounts to determining heat transfers across the gaps between buffer and canister (before buffer swelling is completed), between the canister and the cast iron insert, the insert and the fuel boxes and between the fuel boxes and the fuel rods. In general, heat transfer by both conduction and radiation will play a role in these gaps. The heat flow in the solid metal parts of the components results in only negligible temperature gradients due to the high thermal conductivity of the metals.

Consider the transfer of heat by radiation between two parallel, opposing surfaces S_1 and S_2, separated by a gap of length d, small compared to the linear dimensions of the surfaces. The surfaces have the same area, temperatures T_1 and T_2 and emissivities ε_1 and ε_2, respectively. The radiation energy emitted by surface S1 per unit area is /Carslaw and Jaeger, 1959/

$$\varphi_1^{Rad} = \sigma\varepsilon_1 T_1^4 \tag{7}$$

where $\sigma = 5.6697 \cdot 10^{-8}$ W/(m^{2}K^4) is the Stefan-Boltzmann constant. Since the emissivity also expresses the portion of incident heat radiation absorbed by a surface, the fraction ε_2 is absorbed by S_2 and the fraction $1-\varepsilon_2$ is reflected back to S_1 where the fractionation of absorbed and reflected energy is determined by ε_1 etc. The total transfer of radiation energy from S_1 to S_2 through emission from S_1 followed by successive reflections and absorptions is thus obtained as an infinite geometric progression:

$$\varphi_{1\to 2}^{Rad} = \sigma\varepsilon_1 T_1^4 \varepsilon_2 \left[1 + (1-\varepsilon_1)(1-\varepsilon_2) + (1-\varepsilon_1)^2(1-\varepsilon_2)^2 + \ldots\right] \tag{8}$$

or

$$\varphi_{1\to 2}^{Rad} = \sigma T_1^4 \left(\frac{1}{\varepsilon_1} + \frac{1}{\varepsilon_2} - 1\right)^{-1} \equiv \varepsilon_{12}\sigma T_1^4 \tag{9}$$

Hence the total radiation energy transferred per unit area in the gap is

$$\varphi_{Total}^{Rad} = \sigma\varepsilon_{12}\left(T_1^4 - T_2^4\right) \tag{10}$$

The heat transferred by conduction per unit area is /Carslaw and Jaeger, 1959/

$$\varphi^{Cond} = \frac{(T_1 - T_2)\lambda}{d} \tag{11}$$

where λ is the thermal conductivity in the gap. The heat transferred by these two mechanisms must equal the heat flux per unit area across the gap, φ. We thus obtain

$$T_1^4 + \frac{\lambda}{\sigma\varepsilon_{12}d}T_1 - T_2^4 - \frac{\lambda}{\sigma\varepsilon_{12}d}T_2 - \frac{\varphi}{\sigma\varepsilon_{12}} = 0 \tag{12}$$

Since, for the situations of interest here, T_2 is known, we have a quartic equation in T_1 of the type

$$T_1^4 + a_1 T_1 + a_0 = 0 \tag{13}$$

with

$$a_1 > 0 \tag{14}$$

and

$$a_0 < 0\,. \tag{15}$$

From the solutions /Abramowitz and Stegun, 1970/ to a general quartic equation, the unique real, positive solution to the above special case can be derived as

$$T_1 = \sqrt{\sqrt{\left(\frac{u}{2}\right)^2 - a_0} - \frac{u}{4}} - \sqrt{\frac{u}{4}} \tag{16}$$

where

$$u \equiv \sqrt[3]{s + \sqrt{t^3 + s^2}} + \sqrt[3]{s - \sqrt{t^3 + s^2}}\,, \tag{17}$$

$$s \equiv \frac{a_1^2}{2} \tag{18}$$

and

$$t \equiv -\frac{4a_0}{3}\,. \tag{19}$$

This direct method of calculating the heat transfer across a gap in which both radiation and conduction contribute significantly, reproduces the calculated gap temperature differences, ranging from 0 to 20 K in /Hökmark and Fälth, 2003; Ageskog and Jansson, 1999/. In both these references, an approximate but sufficiently accurate analytical calculation method using effective heat conductivities was used. Benchmarking results against a numerical model is given in section A.4.3.

A.4.2 Application

Due to symmetry, the peak canister surface temperature, T_{CanMax}, will occur at canister mid-height. T_{CanMax} will be slightly over-estimated if the buffer temperature is assumed to be T_{BuffMH}, given by Equation (6), on the entire buffer inner surface, if the canister temperature is assumed to be T_{CanMax} over its entire surface and if the flux across the gap is everywhere assumed to be equal to the average flux over the canister surface, Equation (5) with $d_{CuBuff} = 0$. The interface between canister and buffer is thus represented by two parallel plates of area equal to that of the canister and of temperatures T_{CanMax} and T_{BuffMH} respectively.

The treatment of the gap between the cast iron insert and the copper canister is analogous to that of the gap between the canister and the buffer.

A canister for BWR fuel contains twelve fuel boxes, of height *hBox* = 3.68 m and with cross sectional areas of 0.14 x 0.14 m^2, see Figure A-2. The boxes are housed in channels of quadratic cross section of 0.156 x 0.156 m^2 in the canister insert. For the gaps between the fuel boxes and the cast iron insert inner surfaces, heat transfer is assumed to only take place over the box side surfaces (the x and y directions in Figure A-2), with 1/12 of the total heat power in each box. Again, a constant heat flux across the gap between the box side surfaces and the cast iron insert inner surfaces is assumed.

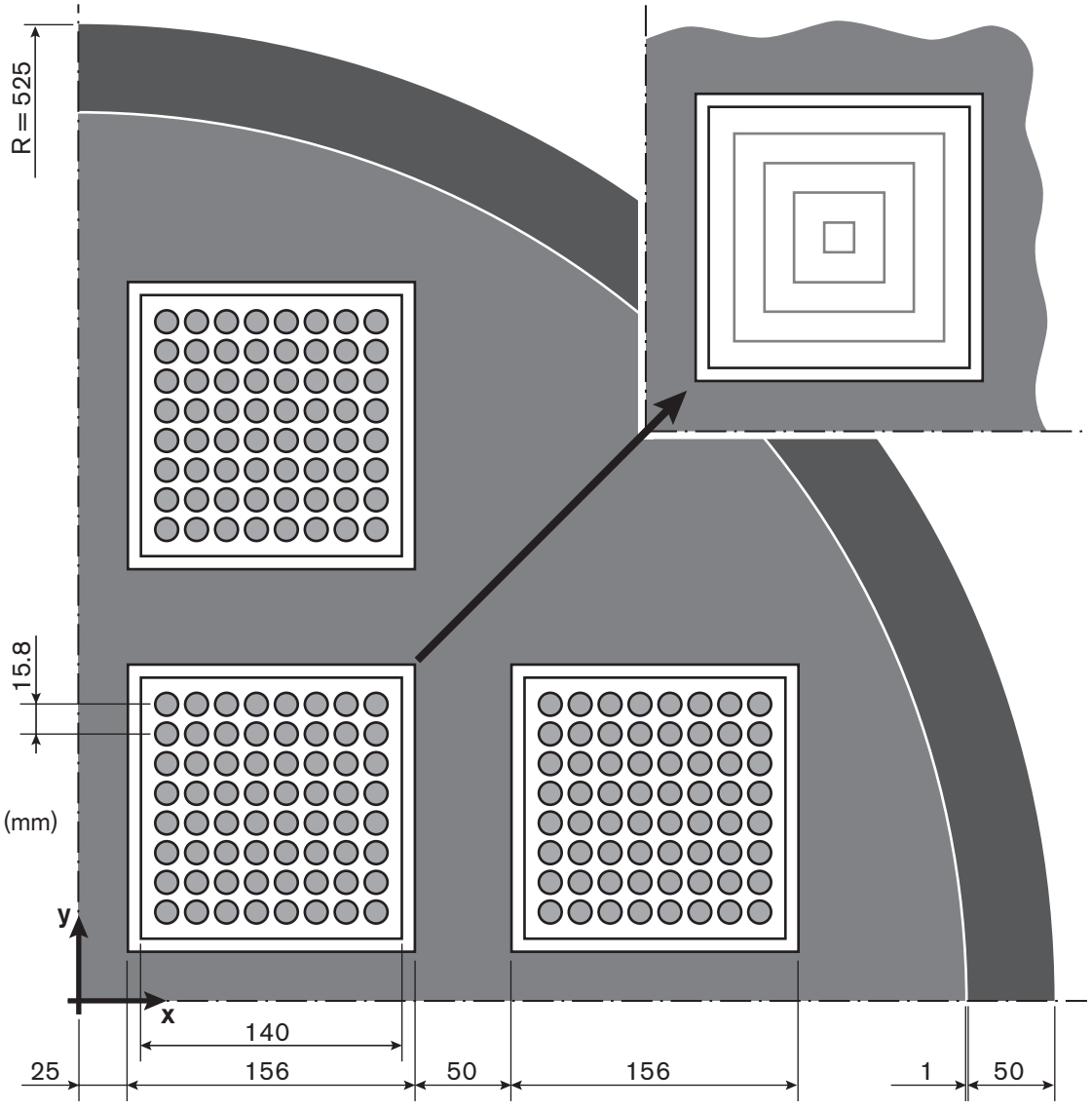

Figure A-2. *Cross section showing a quadrant of the 50 mm thick copper canister, the cast iron insert and three fuel boxes, each with 64 fuel pins. The insert shows how the fuel pins are represented as square line sources in the thermal sub-model. Figure A-3 below shows the temperature along the line y = x calculated with both the 1D thermal sub-model and a 2D numerical model.*

The cross section of the 8 x 8 fuel pins within each fuel box forms a cubic lattice with a centre to centre distance between adjacent pins, *ccPin* = 1.58 cm. In the thermal modelling, the outermost 28 pins are represented as a "pipe" of cubic cross section intersecting the centres of the 28 pins, i.e. by a geometry similar to that of the fuel box, see insert in Figure A-2. The gap between the pipe representing the outer pins and the box is taken as the nearest distance from the centre of an outer pin to the box wall. The flux in the gap is 1/12 of the total flux leaving the canister. The next layer of 20 pins is represented by an analogously defined pipe and with a gap to the outer pins equal to *ccPin*. The flux is here reduced to correspond to that generated by the 6 x 6 pins inside the outermost layer. The remaining two layers are analogously represented by two additional pipes.

A.4.3 Benchmarking

The somewhat crude representation of the fuel pins described above yields results in remarkably good agreement with those from numerical calculations /Renström, 1997/, see Figure A-3. The peak temperature occurs in the central fuel pins whereas the temperature at the centre of the cast iron insert is lower due to the efficient heat conduction in the metal and the absence of heat sources at the centre. The assumed heat power of 2855 W and thus the calculated temperatures are unrealistically high in this example. Vacuum is assumed in the gap between the canister and insert and the copper inner surface has a low emissivity (0.03) yielding a high temperature difference across that gap. All other gaps inside the canister and the fuel boxes are assumed to be air filled with a thermal conductivity of 0.021 W/(m·K). This case thus provides examples of heat transfer in gaps due to both pure radiation and radiation in combination with conduction. The temperature of the cast iron insert is virtually independent of radius in the numerical model results due to the high thermal conductivity of the insert. This justifies the neglect of the thermal gradients in the analytical model.

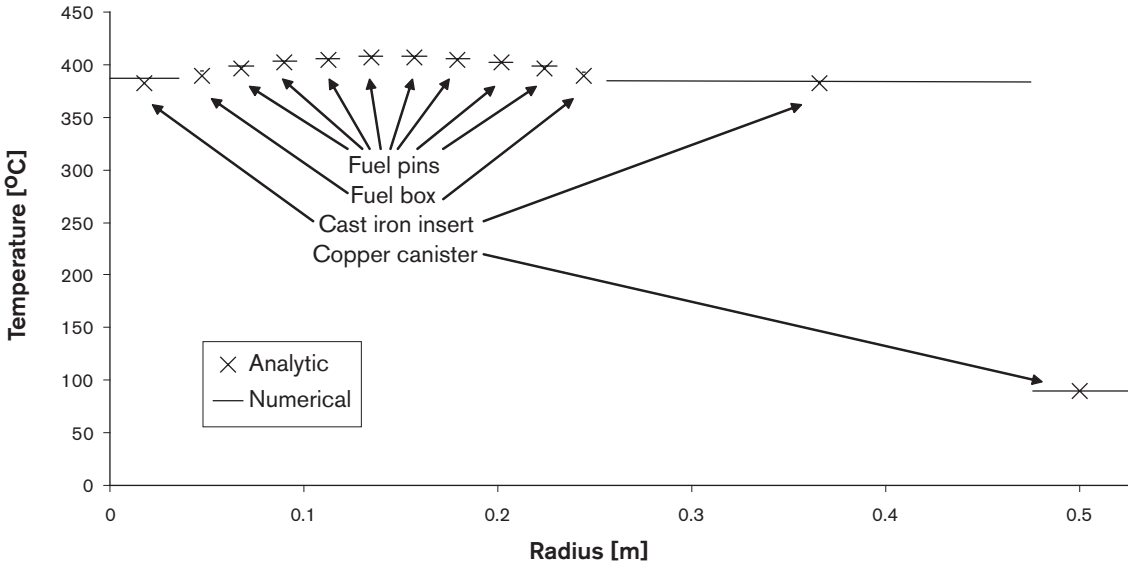

Figure A-3. *Steady state temperature of copper canister (set to 90°C), cast iron insert, fuel boxes and fuel pins along the y = x in Figure A-2. Comparison between the analytic model described here and a 2D numerical model /Renström, 1997/. An unrealistically high residual power of 2855 W was assumed in this example.*

A.5 Integrated thermal calculation

The thermal sub-model was used for an integrated calculation covering the fuel, the canister, the buffer and the host rock. The inner and outer interfaces of the buffer were more realistically represented than in the benchmarking example in section A.3, now with air-filled gaps included between the canister and the buffer and between the buffer and the rock wall. Data for the calculation are given in Table A-1 and the results are shown in Figure A-4.

Table A-1. Thermal sub-model data for the integrated thermal calculation. Geometry data for canister and buffer are given in Figure A-2 and Figure D-1. The canister is assumed to be filled with air.

Repository depth	400 m
Canister spacing	6 m
Tunnel spacing	40 m
Canisters per tunnel	160
Gap copper/buffer, air-filled	0.005 m
Gap buffer/rock, air filled	0.03 m
Initial canister power, P_0	1700 W
Rock thermal conductivity	3.4 W/(m·K)
Rock heat capacity	2.08 MJ/(m^3K)
Temperature at repository depth	12°C
Buffer thermal conductivity	1 W/(m·K)
Emissivity of buffer inner surface	0.88
Emissivity of copper outer surface	0.1
Thermal conductivity in copper/buffer gap	0.03 W/(m·K)
Emissivity of copper inner surface	0.03
Emissivity of cast iron outer surface	0.24
Emissivity of cast iron inner surface	0.3
Emissivity of Zircalloy surfaces	0.4

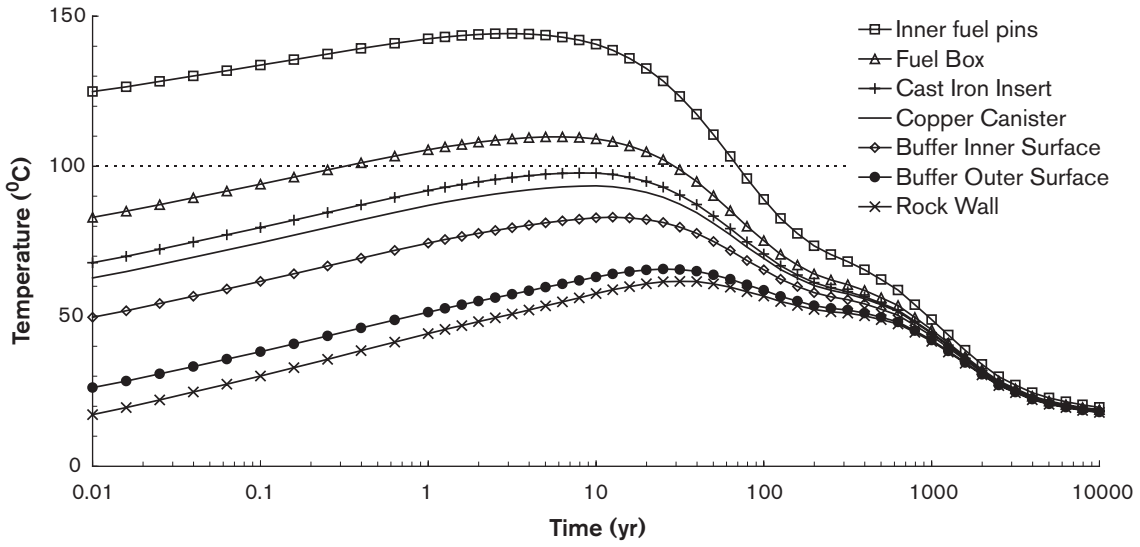

Figure A-4. *Thermal evolution for a number of points at canister mid-height for data given in Table A-1.*

Appendix B

The buffer and backfill rheology model

The following is a more detailed description of the buffer and backfill rheology model. The model describes how the buffer/backfill interface is displaced due to swelling at the end of the water saturation phase of the buffer. The upward swelling will be counter balanced by *i*) friction between the buffer and the walls of the deposition hole and possibly also the walls of the canister and *ii*) pressure from the backfill being contracted by the expanding buffer. The following method to determine the balance point, i.e. the final displacement of the buffer/backfill interface, Δz, is based on the method used in /Börgesson, 1982/:

1. The relationship between Δz and the buffer swelling pressure at the interface is determined.

2. The relationship between Δz and the backfill pressure due to the compression is determined.

3. Using these two relationships, a value of Δz for which the buffer and backfill pressures are equal is determined numerically.

In order to perform the calculation, the relationship between buffer density and swelling pressure must be known. The swelling pressure at saturated conditions, P_s, is primarily determined by the cation exchange capacity of the clay, *CEC*, the density of the clay, ρ_{Clay}, and of the ion concentration of the surrounding groundwater, *C*. /Karnland et al, 2002/ gives the swelling pressure as a function of density for fresh water as

$$P_s^{Fresh} = AT\left(\exp\left(B\frac{\rho_{solid}\left(\rho_{clay}-\rho_{water}\right)}{\rho_{water}\left(\rho_{solid}-\rho_{clay}\right)}\right)-1\right) \qquad (20)$$

where *A* and *B* are fitting parameters that can in principle be determined from basic thermodynamic and microstructural properties of the clay, *T* is the absolute temperature and ρ_{clay}, ρ_{water} and ρ_{solid} are the densities of the saturated clay, of water and of the solid clay particles, respectively. The uppermost curve in Figure B-1 is a representation of Equation (20).

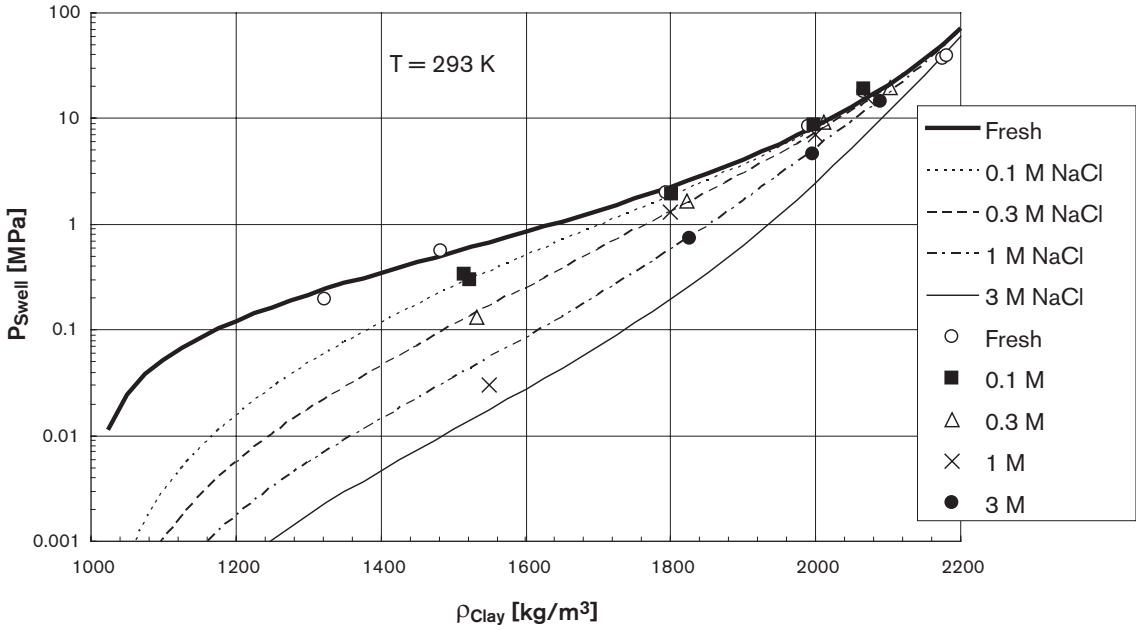

Figure B-1. *Calculated and experimentally determined values of P_s as a function of density for several external solution concentrations.*

For a saline groundwater, the swelling pressure will be reduced due to osmotic effects as the full external ion concentration may not enter the buffer pore water, so prevented by ion activity constraints leading to a Donnan equilibrium /Karnland et al, 2002/. For an external NaCl salt solution of concentration C [M] surrounding a buffer with Na^+ as the adsorbed cation, the following relationship, based on activity equilibrium between ions in the pore water and in the external solution, gives the swelling pressure /Karnland et al, 2002/:

$$P_s = \sqrt{\left(P_s^{Fresh}\right)^2 + \left(2RTC\alpha_d\right)^2} - 2RTC\alpha_d \tag{21}$$

where P_s is the swelling pressure in kPa, R = 8.314 J/(K·mole) is the gas constant and α_d [-] is the tabulated degree of dissociation for the external NaCl solution of concentration C given approximately by

$$\alpha_d \approx 10^{\frac{-0.34\sqrt{C}}{1+1.83\sqrt{C}}} + 0.03C \tag{22}$$

Figure B-1 shows calculated and experimentally determined values of P_s for a number of solution concentrations over density ranges of interest. These relationships are one of the prerequisites for the swelling calculation.

The clay buffer in the deposition hole is (partially) unconfined only in the upward z direction, in which it may expand by compressing the tunnel backfill. The upward swelling will be counteracted by friction against the wall of the deposition hole. For a swelling pressure P_s, the friction force over a length Δz will be /Börgesson, 1982/

$$F = \Delta z 2\pi r_{DepHole} \tan\left(\varphi_{Buff}\right) P_s(z) \tag{23}$$

where φ_{Buff} is the friction angle between the clay and the rock wall and $r_{DepHole}$ is the radius of the deposition hole. At equilibrium, the net force on the element of thickness Δz must be zero. Thus

$$\pi r_{DepHole}^2 \left[P_s(z+\Delta z) - P_s(z)\right] = -\Delta z 2\pi r_{DepHole} \tan(\varphi_{Buff}) P_s(z) \tag{24}$$

or

$$\frac{dP_s(z)}{dz} = -\frac{2\tan(\varphi_{Buff})}{r_{DepHole}} P_s(z) \tag{25}$$

i.e.

$$P_s(z) = P_s(z_0)\exp\left[-\frac{2\tan(\varphi_{Buff})(z-z_0)}{r_{DepHole}}\right] \qquad z > z_0 \tag{26}$$

Generalising to include also friction against the canister of radius r_{Can} we obtain, assuming the same friction angle as above

$$P_s(z) = P_s(z_0)\exp\left[-\frac{2\tan(\varphi_{Buff})(z-z_0)}{r_{DepHole} - r_{Can}}\right] \tag{27}$$

According to Eqs. (20) and (21), the clay density can be expressed as a function of the swelling pressure for the saturated clay, so that we have in general

$$\rho_{Clay}(z) = f(P_s(z)) \tag{28}$$

The total clay mass will increase as water is absorbed in the swelling process. However, the total clay dry mass will be unchanged. The total dry mass, M_{dry}^{Tot}, is

$$M_{dry}^{Tot} = \left(h_{Buffer}\pi r_{dephole}^2 - h_{Can}\pi r_{can}^2\right)\rho_{dry}^0 \tag{29}$$

where h_{Buffer} is the height of the clay buffer before swelling, h_{Can} is the height of the canister and ρ_{dry}^0 is the buffer dry density before swelling. The dry density is related to the clay density through

$$\rho_{dry} = \rho_{solid}\frac{\rho_{Clay} - \rho_{water}}{\rho_{solid} - \rho_{water}} \tag{30}$$

The net movement of the canister is assumed to be negligible during swelling as indicated by detailed modelling of the swelling process /Börgesson and Hernelind, 1999/. Denoting by z_{CanTop} the z co-ordinate for the top of the canister and assuming that the swelling starts at $z_0 < z_{CanTop}$, the total dry mass above z_0 before swelling is

$$M_0 = \pi\rho_{dry}^0\left[\left(z_{CanTop} - z_0\right)\left(r_{dephole}^2 - r_{can}^2\right) + \left(h_{buffer} - z_{CanTop}\right)r_{dephole}^2\right] \tag{31}$$

where ρ_{dry}^{0} is the initial dry density, which is independent of z. After swelling, we obtain for the dry mass between z and z_{CanTop}

$$M_1 = \pi\left(r_{dephole}^2 - r_{can}^2\right)\rho_{solid} \int_{z_0}^{z_{CanTop}} \frac{\rho_{Clay}(z) - \rho_{water}}{\rho_{solid} - \rho_{water}} dz \tag{32}$$

The mass above the canister after swelling, M_2, must be such that $M_2 = M_0 - M_1$, i e swelling occurs to the distance z_{max} determined by the equation

$$M_0 - M_1 = \pi\left(r_{dephole}^2 - r_{can}^2\right)\rho_{solid} \int_{z_{CanTop}}^{z_{\max}} \frac{\rho_{Clay}(z) - \rho_{water}}{\rho_{solid} - \rho_{water}} dz \tag{33}$$

In order to perform the integration, Equation (21) is solved for ρ_{Clay} utilising Equation (20) and, using Equation (27), an expression for $\rho_{Clay}(z)$ for Equation (32) is obtained. The variable z_{max} is then found by numerical integration.

The backfill consists of a cylindrical part filling the top portion of the deposition hole and the material filling the tunnel. As the buffer exerts an upward force, F, on the backfill due to the buffer swelling, the resulting stress in the tunnel material is assumed to be distributed over a radius that increases linearly with z /Börgesson, 1982/. This means that the part of the backfill above the deposition hole that contributes in the mechanical interaction with the buffer takes the form of a truncated cone with the radius of its lower, smaller end surface equal to that of the deposition hole. The radius of the backfill material taking up the stress as a function of z is thus described by

$$r_{Backfill}(z) = \begin{cases} r_{dephole} & h_{buffer} < z \le h_{dephole} \\ r_{dephole} + \left(z - h_{dephole}\right)S & h_{dephole} < z < h_{dephole} + h_{tunnel} \end{cases} \tag{34}$$

where the constant S describes the linear increase in radius due to the distribution of stress in the tunnel material and h_{tunnel} is the height of the tunnel. The compression, Δz, of the contributing backfill material is obtained by integration along the z axis:

$$\Delta z = \frac{F}{M} \int_{h_{Buffer}}^{h_{dephole}+h_{tunnel}} \frac{dz}{\pi\, r_{backfill}^2(z)} \tag{35}$$

where M [MPa] denotes the compressibility of the backfill material, assumed constant since it depends only weakly on stress over the range of stress of concern here. Inserting Equation (34) into Equation (35) yields

$$\Delta z = \frac{P_s(z_{\max}) - \sigma_{Backfill}^{0}}{M}\left[h_{dephole} - h_{buffer} + \left(\frac{r_{dephole} h_{tunnel}}{r_{dephole} + h_{tunnel} S}\right)\right] \tag{36}$$

where

$$P_s(z_{\max}) - \sigma_{Backfill}^{0} = F / \pi\, r_{dephole}^2 \tag{37}$$

is the swelling pressure exerted by the buffer on the backfill reduced by the initial stress in the backfill. This treatment neglects friction between the backfill and the wall of the deposition hole. If friction is included, Equation (36) is modified:

$$\Delta z = \frac{P}{M}\left[\frac{r_{DepHole}}{2\chi}\left(1-\exp\left(-\frac{2\left(h_{dephole}-h_{buffer}\right)\chi}{r_{DepHole}}\right)\right)+ \exp\left(-\frac{2\left(h_{dephole}-h_{buffer}\right)\chi}{r_{DepHole}}\right)\left(\frac{r_{dephole}h_{tunnel}}{r_{dephole}+h_{tunnel}S}\right)\right] \quad (38)$$

where

$$\chi = \tan\left(\varphi_{Backfill}\right)K_0 \quad (39)$$

Here, $\varphi_{Backfill}$ is the friction angle between the backfill and the deposition hole wall and $K_0 \approx 0.5$ describes, for an applied vertical stress in the backfill material, the fraction of this stress that will develop in the horizontal direction /Börgesson, 2004/. Equation (39), which differs from Equation (36) only for the part of the backfill in the deposition hole, was derived analogously to Equation (27).

The above results are used in the following way to determine the displacement of the buffer/backfill interface Δz:

1. Assume a value z_0 below which no buffer swelling occurs.
2. Determine the corresponding value of Δz for the buffer by numerical integration of Equation (33).
3. Determine the buffer swelling pressure at the interface for this value of Δz using Equation (27).
4. Determine the value of Δz in the backfill for the same pressure using Equation (36) or (38).
5. Adjust z_0 to improve the matching of the Δz values for the buffer and the backfill until a sufficient agreement has been obtained.

Around five cycles in the above scheme yielded a fully sufficient accuracy of Δz. As an accuracy check of the numerical integration, the total buffer dry mass before and after swelling are compared and the relative error is typically around 10^{-6}.

Note that the treatment is only valid for the initial swelling. If e.g. a ground water of higher salinity would intrude after completed initial swelling, resulting in lower swelling pressures in the buffer according to Equation (21), the initial expansion would not be simply reversed.

B.1 Example and benchmarking calculations

The calculated buffer expansion into the backfill is 9.6 cm using the system sub-model and 8 cm using the process model /Börgesson and Hernelind, 1999/. This is seen as a reasonable result, since it errs on the pessimistic side and since the process model was not optimised to handle the mechanical interactions involved. The buffer density in the z direction decreases in similar manners for the two models. In this benchmarking exercise a simpler swelling equation was used, since this corresponds more closely to the equation used by the process model:

$$\rho_{Clay}(z) = (103 \ \ln P_s(z) + 1786)\text{kg/m}^3 \tag{40}$$

For this case, the integral in Equation (33) is solved analytically.

The rheology sub-model was also used to calculate the buffer expansion for the data in Table B-1. Equation (20) was used for the relationship between swelling pressure and density. Figure B-2 shows the results for this case. Note that the tolerances of the buffer density, 2000±50 kg/m^3, yields swelling pressures between 5.8 and 13 MPa.

Table B-1. Buffer/Backfill rheology sub-model data for the central case. Geometry data for buffer and backfill are given in Figure D-1**.**

Initial clay density, ρ	2000±50 kg/m^3
Buffer temperature, T	50°C
Friction angle buffer/deposition hole, Φ	10°
Friction angle backfill/deposition hole	30°
Compression modulus of backfill, M	40 MPa

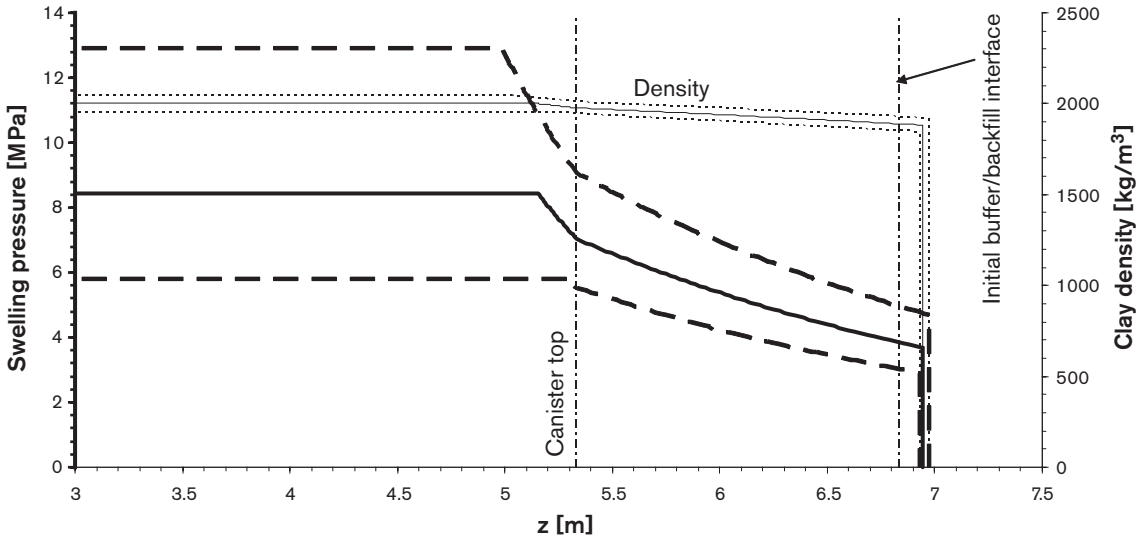

Figure B-2. *Swelling pressure (thick curves) and clay density along vertical axis of deposition hole after initial swelling. Solid line: Initial density 2000 kg/m^3; Dashed lines: initial densities 1950 and 2050 kg/m^3. Note the large effect on swelling pressure caused by the small variation in density.*

Appendix C

The buffer chemistry model

All equations for the buffer chemical model are taken from the corresponding process model /Bruno et al, 1999/, where the system of equations is solved by a general purpose code for chemical applications. The following is a listing of the equations and a description of the calculation algorithm developed specifically for this sub-model. The model calculates the equilibrium between ionic species (Na^+, Ca^{2+} and Mg^{2+}) dissolved in the buffer pore water and ions adsorbed to the exchange sites (X) of the clay according to

$$\frac{x_{CaX_2}[Na^+]^2}{(x_{NaX})^2[Ca^{2+}]} = k_1 \frac{f_2}{(f_1)^2} \tag{41}$$

$$\frac{x_{MgX_2}[Na^+]^2}{(x_{NaX})^2[Mg^{2+}]} = k_2 \frac{f_2}{(f_1)^2} \tag{42}$$

where $[\cdot]$ denotes the concentration of a dissolved species in the pore water and x denotes the molar fraction of a surface species. The entities k_1 and k_2 are the equilibrium constants for the reactions in question. The activity coefficients f_z compensate the equilibrium constants for the ionic strength of the solution according to Davies' approximation /Davies, 1962/:

$$f_z = 10^{-z^2 0.51\left(\frac{\sqrt{I}}{1+\sqrt{I}} - 0.2I\right)} \tag{43}$$

where z denotes the number of electron charges of an interacting dissolved species and I is the ionic strength of the solution obtained from the concentrations and charges of the dissolved species:

$$I = \tfrac{1}{2}\sum_i C_i (z_i)^2 \tag{44}$$

Protonation/deprotonation of clay mineral surface edge sites, ≡SOH, occurs according to:

$$\frac{[\equiv SOH_2^+]}{[\equiv SOH][H^+]} = k_3 f_1 \tag{45}$$

$$\frac{[\equiv SOH]}{[\equiv SOH^-][H^+]} = k_4 f_1 \tag{46}$$

The dissolution or precipitation of calcite is governed by

$$\frac{[Ca^{2+}][HCO_3^-]}{[H^+]} = k_5 \frac{1}{f_2} \tag{47}$$

Protonation/deprotonation of carbonate is governed by

$$\frac{[HCO_3^-][H^+]}{[H_2CO_3]} = k_6 \frac{1}{(f_1)^2} \tag{48}$$

$$\frac{[CO_3^{2-}][H^+]}{[HCO_3^-]} = k_7 \frac{1}{f_2} \tag{49}$$

Finally, the ion product of water yields the condition

$$[OH^-][H^+] = k_8 \frac{1}{(f_1)^2} \tag{50}$$

Any dissolved oxygen in the pore water is assumed to react with pyrite, $FeS_2(s)$, if this mineral is present:

$$FeS_2(s)+15/4O_2(g) + 7/2H_2O \rightarrow Fe(OH)_3(s) + 2\,SO_4^{2-} +4H^+$$

yielding 16/15 moles of H^+ for one mole of $O_2(g)$.

The compositions of the pore water and the solid phases before equilibrium are known and the system is subject to the following mass balance conditions before and after equilibration:

$$H^{Total} = [H^+]+[\,HCO_3^-\,]+[\equiv SOH]+2[\,\equiv SOH_2^+\,] + 2[H_2CO_3]-[OH^-]+16/15[O_2(g)] \tag{51}$$

$$HCO_3{}^{Total} = [\,HCO_3^-\,]+[H_2CO_3] + [\,CO_3^{2-}\,]+[CaCO_3(s)] \tag{52}$$

$$Na^{Total} = [Na^+]+ x_{NaX}\,CEC \tag{53}$$

$$Ca^{Total} = [Ca^{2+}]+ x_{CaX_2}\,CEC/2+ [CaCO_3(s)] \tag{54}$$

$$Mg^{Total} = [Mg^{2+}]+ x_{MgX_2}\,CEC/2 \tag{55}$$

$$\equiv SO^{Total} = [\equiv SO^-]+[\equiv SOH]+[\,\equiv SOH_2^+\,] \tag{56}$$

$$1 = x_{NaX} + x_{CaX_2} + x_{MgX_2} \tag{57}$$

$[CaCO_3(s)]$ denotes the amount of undissolved calcite in a bentonite volume corresponding to one litre of pore water and CEC is the cation exchange capacity of the clay.

The above system of eight equilibrium conditions, seven mass balance conditions and 15 variables to be determined is solved in the following nine steps of simple algebraic manipulations:

1. Start approximations of $[H^+]$ and of the ionic strength of the solution are estimated;

2. $[OH^-]$ then follows from Equation (50);

3. [≡SO^-], [≡SOH] and [$\equiv SOH_2^+$] are obtained from (45), (46) and (56);

4. [HCO_3^-], [H_2CO_3] and [CO_3^{2-}] now follow from (48), (49) and (51);

5. [$CaCO_3$(s)] follows from (52);

6. [Ca^{2+}] follows from (47);

7. [CaX_2] is obtained from (54);

8. [Na^+] and [NaX] follow from (41) and (53) and, finally,

9. [Mg^{2+}] and [MgX_2] are obtained from (42) and (55).

Since the value of [H^+] is imposed in the first step, the system is over-determined and the condition (57), which was not used above, is in general not fulfilled, i.e. the correct equilibrium concentrations are not obtained with the assumed value of [H^+]. The imbalance of Equation (57) is now used as an implication of how to improve the estimate of [H^+]. The improved value of [H^+] and the ionic strength of the calculated concentrations are used in a refined determination of the variables and this is repeated until a required accuracy for the condition (57) is obtained. The chemical equilibrium for the time step under consideration has then been determined. The concentration changes between time steps are small and the value of [H^+] in step N is thus a good start approximation for step N+1, yielding a solution with required accuracy after typically only two iterations in each time step. The relative error of e.g. [H^+] is then less than typically 10^{-3}.

The variables [SO_4^{2-}] and [FeS_2(s)] after equilibration are simply the initial concentrations modified by the (possible) dissolution of pyrite described above. The oxygen fugacity, f(O_2), and the redox parameter pe after equilibration are obtained as

$$f(O_2) = k_9[SO_4^{2-}]^{8/15}[H^+]^{16/15} \quad (58)$$

$$pe = ¼\ {}^{10}\log(f(O_2)) - pH - ¼\ {}^{10}\log k_{Eh} \quad (59)$$

where k_{Eh} is a constant.

If the buffer is depleted of pyrite, the term containing [O_2(g)] is left out in Equation (51). If the buffer is depleted of calcite, the condition (47) is no longer fulfilled and step 5 above is not defined. The system is then described by two independent, simpler systems of equations that are both solved by schemes similar to that used above, but consisting of fewer steps.

C.1 Benchmarking

The chemical evolution of the buffer was modelled using groundwater compositions for three different sites. The master variables pe and pH, cationic species adsorbed to montmorillonite, calcite content and a number of other variables were determined as functions of time and compared to the corresponding process model results /Bruno et al, 1999/, see Figure C-1 showing the comparison for one of the sites. The evolutions of

the other two sites are in some respects different, but similarly modelled by the system and process models. From the point of view of long-term safety, the minor discrepancies between the models in these three examples are negligible.

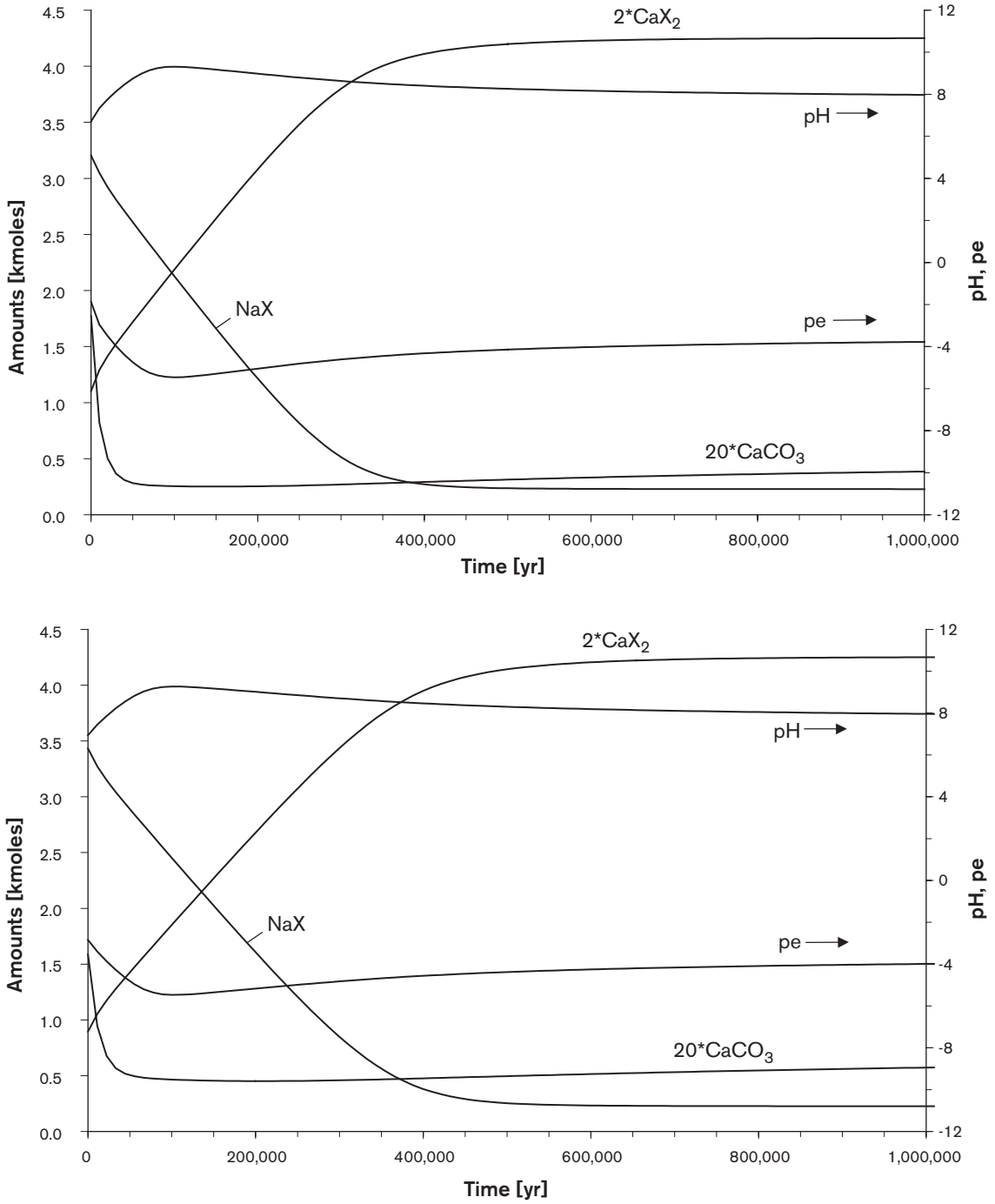

Figure C-1. *Buffer chemistry model benchmarking results for system sub-model (upper) and process model (lower). The figure shows the master variables pH and pe as well as the exchange of Na^+ ions for Ca^{2+} ions at the surface positions, X, of the clay mineral, driven initially partly by the dissolution of calcite, $CaCO_3$.*

Appendix D

The canister corrosion sub-model

The following is a more detailed description of the copper corrosion sub-model. The model handles corrodants supplied by the flowing groundwater as well as corrodants initially present in the buffer. In general, corrosion is limited by the rate of transport of corrodants to the canister whereas the corrosion reactions are assumed to be instantaneous.

D.1 Corrodants in groundwater

Corrodants dissolved in the groundwater are assumed to access the buffer and canister through fractures intersecting the deposition hole and through the excavation damaged zone in the floor of the deposition tunnel above the deposition hole, Figure D-1.

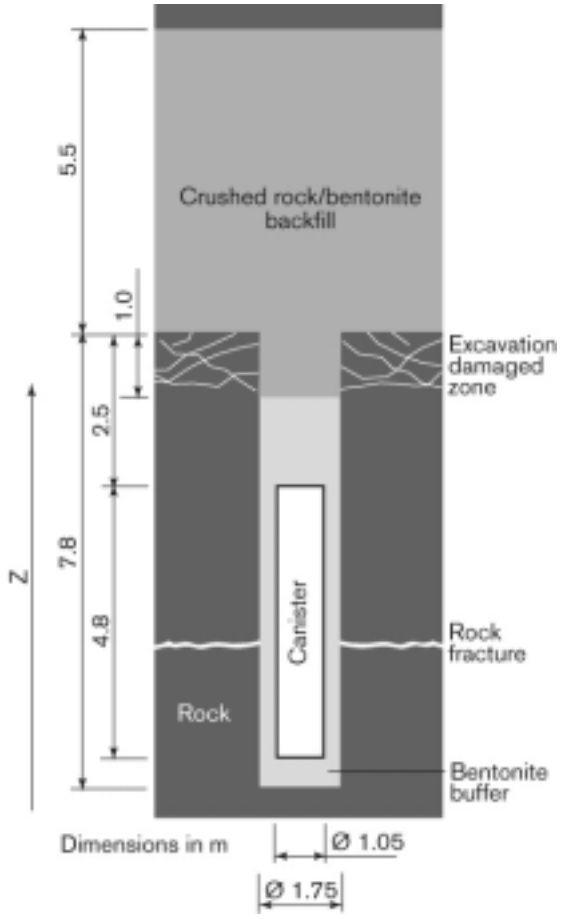

Figure D-1. *Corrodants in groundwater entering from the excavation damaged zone, EDZ, will attack the canister top whereas those entering from an intersecting horizontal fracture will diffuse through the bentonite and corrode a section of the canister lateral surface of height roughly equal to the thickness of the buffer surrounding the canister lateral surface. Corrodants initially in the buffer will diffuse to and attack both the lateral surface and the top.*

At steady state, the diffusional transport of corrodants from the groundwater of a certain corrodant concentration to the canister surface where the concentration is assumed to be zero due to instantaneous consumption of the corrodants, can be described by a set of transport resistances. The treatment is similar to an analytical treatment of transport of radionuclides out from a defective canister summarised in /Hedin, 2002/.

At the entrances to the deposition hole, the transport may be hindered both for geometrical reasons when the fracture is narrow, and due to the limited capacity of the slowly flowing groundwater to carry corrodants to the buffer.

The transport resistance between the buffer and a narrow intersecting fracture in the rock can be approximated by

$$R^{Diff}_{Buffer\,/\,Fracture} = F\frac{\delta}{A_f D_e^{Buff}} \tag{60}$$

where δ is the fracture aperture, A_f is the fracture area, D_e^{Buff} is the element specific effective diffusivity in the buffer and F is a geometrical factor /Neretnieks, 1986a/.

The limited capacity of the slowly flowing groundwater in the surrounding rock to carry material to the deposition hole may be expressed in terms of a transport resistance at the entrance as

$$R^{q}_{Fracture} = \frac{1}{A_q\sqrt{q}} \tag{61}$$

where q is the water flux at the deposition hole and A_q is a lumped parameter determined by geometrical properties of the fracture and the diffusivity of the solute in the groundwater. The relationship underlying Equation (61) was derived /Neretnieks, 1979/ through boundary layer theory to solve the equations for diffusive transport to the passing water.

The total entrance resistance for a narrow fracture is thus

$$R_{Fracture} = R^{q}_{Fracture} + R^{Diff}_{Buffer\,/\,Fracture} \tag{62}$$

whereas for the broader excavation-damaged zone the geometrical resistance is assumed negligible; thus,

$$R_{EDZ} = R^{q}_{EDZ} \tag{63}$$

Species entering through the excavation damaged zone will have to pass the top section of the buffer to reach the canister. This section of the buffer offers a diffusional transport resistance

$$R_{BuffTop} = \frac{L}{\pi r^2_{DepHole} D_e} \tag{64}$$

These species are assumed to attack the top surface of the canister.

Species entering through intersecting fractures will pass the portion of the buffer surrounding the lateral surface of the canister and subsequently attack this surface. The transport resistance in the buffer is concentrated around the fracture as expressed by Equation (62).

The relative canister corrosion rate, $Rate_{Rel}$, varying in the vertical direction due to the vertical spread of corrodants in the buffer, can be estimated using the simplified expression /Neretnieks, 1986a/

$$Rate_{Rel} = \frac{\delta}{2h_{Can}} + 2\sum_{m=1}^{\infty} \frac{\cos(m\pi\, z / h_{Can})\sin(m\,\pi\,\delta / h_{Can})}{m\pi\,\cosh\left(m\pi\left(r_{DepHole} - r_{Can}\right)/ h_{Can}\right)} \tag{65}$$

An evaluation of this expression demonstrates that the highest corrosion rate, occurring at the same height as the fracture, is around 7 times the average corrosion rate over the canister surface. We thus obtain, for a groundwater corrodant concentration of C, a corrosion rate of the lateral surface at the fracture, $Rate_{Lateral}$

$$Rate_{Lateral} = \frac{7C}{R_{Fracture}\, 2\pi r_{Can} h_{Can}} \tag{66}$$

and for corrosion of the top surface, $Rate_{Top}$,

$$Rate_{Top} = \frac{C}{\left(R_{EDZ} + R_{BuffTop}\right)\pi r_{Can}^2} \tag{67}$$

D.2 Corrodants initially in buffer

The buffer contains a certain concentration of pyrite, FeS_2, corresponding to an equivalent concentration of sulphide, C_{HS}^{Buff} [kg/m^3], that is sufficient to uphold a constant concentration of sulphide in the buffer pore water, determined by the chemical environment in the buffer. Sulphide will however be consumed by corrosion of the copper canister, meaning that the buffer contents of solid, immobile pyrite will be depleted from the buffer/canister interface and outward. Since the initial equivalent concentration C_{HS}^{Buff} is considerably higher than the concentration limit C_{HS}^{PW}, the situation can, in one dimension, be described as a distance x from the canister at time t, within which the buffer is depleted of pyrite. Between the canister surface and x, sulphide will diffuse to the canister, further depleting the buffer of pyrite. The rate at which the depletion front moves is determined by the flux of sulphide diffusing from the front to the canister

$$\varphi(x) = C_{HS}^{PW}\,\frac{D_e A}{x} \tag{68}$$

and the rate at which the front moves given a certain flux

$$\frac{dx}{dt} = \frac{\varphi(x)}{C_{HS}^{Buff} A} \tag{69}$$

Inserting Equation (68) in Equation (69) and integrating yields

$$x(t) = \sqrt{\frac{2D_e C_{HS}^{PW}}{C_{HS}^{Buff}} t} \qquad 0 < x < \mathrm{L} \tag{70}$$

An identical result has previously been reached with a similar derivation /Neretnieks, 1986b/. Applying this to the bentonite surrounding the lateral surface of the canister yields a corroded amount of copper according to

$$M(t) = H_{Can}\pi\left[(r_{Can} + x(t))^2 - r_{Can}^2\right] 2C_{HS}^{Buff}; \qquad x(t) \le d_{Buff} \tag{71}$$

Similarly, corrodants in the top section of the buffer will corrode the canister top according to

$$M(t) = \pi r_{Can}^2 x(t) 2C_{HS}^{Buff}; \qquad x(t) \le H_{CanTop} \tag{72}$$

The same derivation can be applied to a cylindrical geometry, representing the situation for the lateral surface of the canister more correctly:

$$t(r) = \frac{C_{HS}^{Buff}}{D_e C_{HS}^{PW}}\left[\frac{r^2}{2}\left(\ln\left(\frac{r}{r^{Can}}\right) - \frac{1}{2}\right) + \frac{\left(r^{Can}\right)^2}{2}\right] \qquad r^{Can} < r < r^{DepHole} \tag{73}$$

where r is the distance of the front from the canister surface. For this case, the expression can not be solved for r.

Appendix E

The canister interior sub-model

As mentioned in section 2.6, this sub-model handles water ingress from the buffer, driven by the pressure difference between the groundwater and the canister interior, build-up of water, both in the annulus between copper canister and the cast iron insert and inside the insert, and anaerobic corrosion of the insert leading to hydrogen gas formation and a consequent build-up of an internal gas pressure. The gas pressure may cause expulsion of gas and water from the canister interior.

The evolution is described, in the sub-model and the corresponding process model, by the same eight time-dependent variables and the evolution of the variables is governed by the same set of coupled differential equations, see further /Bond et al, 1997/. Both models solve the system numerically in a number of time steps. The method used by the system sub-model however differs from that used by the process model in mainly two respects:

1. The method is explicit i.e. the state at time step N+1 is calculated based on reaction rates etc in step N whereas the process model uses a more computationally demanding and slightly more accurate implicit scheme.

2. The time-step of the system sub-model is typically one hundred years, which is two orders of magnitude larger than that of the process model, again with a minor sacrifice of accuracy. The long time-step is achieved by introducing specifically designed damping features, effectively preventing oscillations in the solution.

E.1 Benchmarking

The canister interior evolution was modelled for four different cases and compared to the corresponding process model results /Bond et al, 1997/, see Figure E-1, showing the comparison for one case and for a few essential variables.

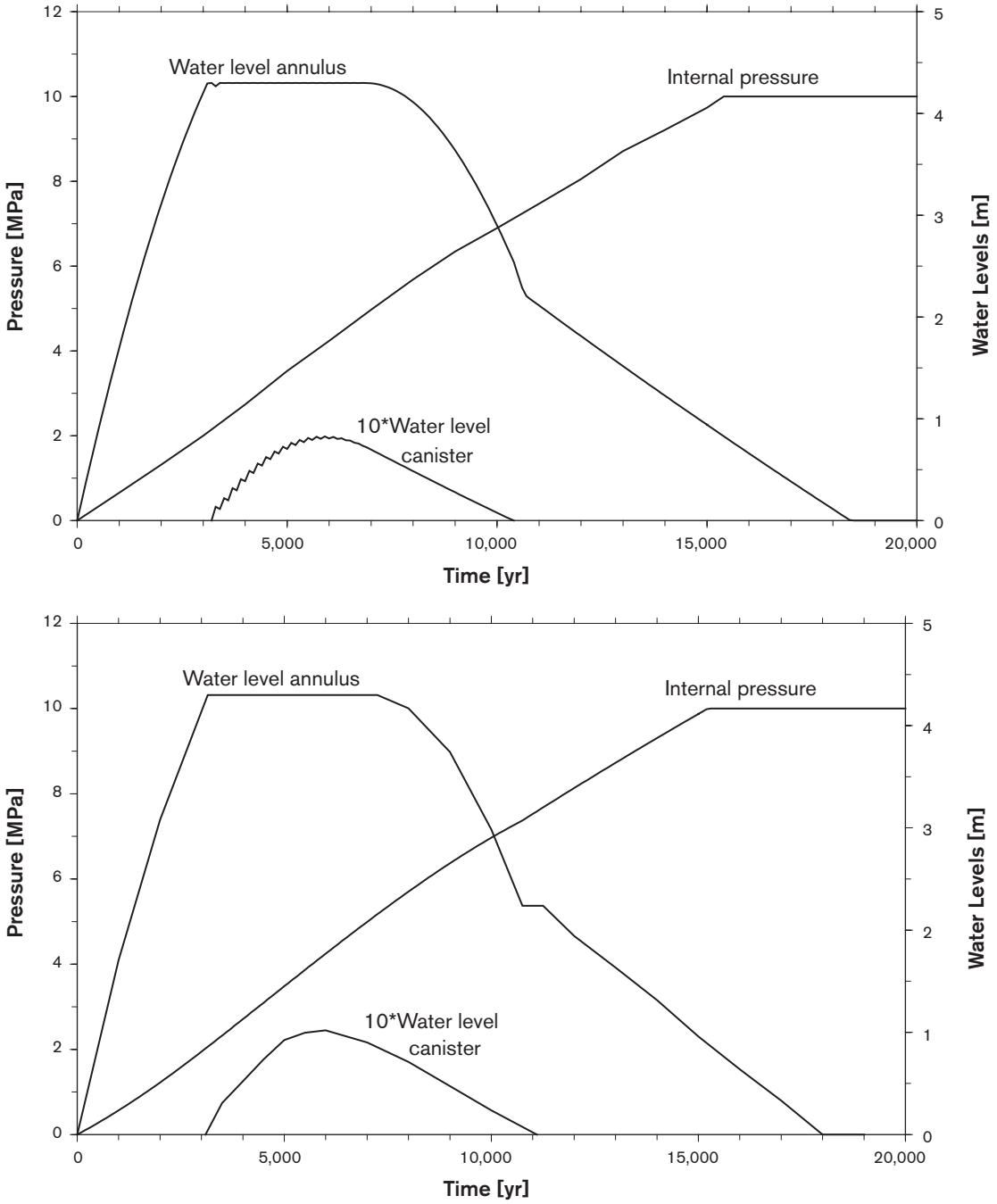

Figure E-1. *Canister interior model benchmarking results showing water levels inside canister insert and in annulus between insert and copper shell for system sub-model (upper) and process model (lower).*